Title

Deep Learning Automated Background Phase Error Correction for Abdominopelvic 4D Flow MRI.

Journal

Radiology, 302(3)

ISSN

0033-8419

Authors

You, Sophie
Masutani, Evan M
Alley, Marcus T
et al.

Publication Date

2022-03-01

DOI

10.1148/radiol.2021211270

Peer reviewed

Radiology

Deep Learning Automated Background Phase Error Correction for Abdominopelvic 4D Flow MRI

*Sophie You, BA** • *Evan M. Masutani, CPhil** • *Marcus T. Alley, PhD* • *Shreyas S. Vasanawala, MD, PhD* • *Pam R. Taub, MD* • *Joy Liau, MD, PhD* • *Anne C. Roberts, MD* • *Albert Hsiao, MD, PhD*

From the School of Medicine (S.Y., E.M.M.), Department of Cardiovascular Medicine (P.R.T.), and Department of Radiology (J.L., A.C.R., A.H.), University of California, San Diego, 9300 Campus Point Dr, La Jolla, CA 92037-0841; and Department of Radiology, Stanford University School of Medicine, Stanford, Calif (M.T.A., S.S.V.). Received May 18, 2021; revision requested July 23; revision received August 19; accepted October 4. **Address correspondence to** A.H. (e-mail: *hsiao@ucsd.edu*).

E.M.M. is supported by a predoctoral fellowship from the American Heart Association and the University of California San Diego Medical Scientist Training Program (NIH/NIHGMS T32GM007198). S.Y. is supported by the Altman Clinical and Translational Research Institute MedGap Program.

* S.Y. and E.M.M. contributed equally to this work.

Conflicts of interest are listed at the end of this article.

See also the editorial by Roldán-Alzate and Grist in this issue.

Radiology 2022; 302:584–592 • https://doi.org/10.1148/radiol.2021211270 • Content codes: GI AI

Background: Four-dimensional (4D) flow MRI has the potential to provide hemodynamic insights for a variety of abdominopelvic vascular diseases, but its clinical utility is currently impaired by background phase error, which can be challenging to correct.

Purpose: To assess the feasibility of using deep learning to automatically perform image-based background phase error correction in 4D flow MRI and to compare its effectiveness relative to manual image-based correction.

Materials and Methods: A convenience sample of 139 abdominopelvic 4D flow MRI acquisitions performed between January 2016 and July 2020 was retrospectively collected. Manual phase error correction was performed using dedicated imaging software and served as the reference standard. After reserving 40 examinations for testing, the remaining examinations were randomly divided into training (86% [85 of 99]) and validation (14% [14 of 99]) data sets to train a multichannel three-dimensional U-Net convolutional neural network. Flow measurements were obtained for the infrarenal aorta, common iliac arteries, common iliac veins, and inferior vena cava. Statistical analyses included Pearson correlation, Bland-Altman analysis, and *F* tests with Bonferroni correction.

Results: A total of 139 patients (mean age, 47 years ± 14 [standard deviation]; 108 women) were included. Inflow-outflow correlation improved after manual correction ($\rho = 0.94$, $P < .001$) compared with that before correction ($\rho = 0.50$, $P < .001$). Automated correction showed similar results ($\rho = 0.91$, $P < .001$) and demonstrated very strong correlation with manual correction ($\rho = 0.98$, $P < .001$). Both correction methods reduced inflow-outflow variance, improving mean difference from −0.14 L/min (95% limits of agreement: −1.61, 1.32) (uncorrected) to 0.05 L/min (95% limits of agreement: −0.32, 0.42) (manually corrected) and 0.05 L/min (95% limits of agreement: −0.38, 0.49) (automatically corrected). There was no significant difference in inflow-outflow variance between manual and automated correction methods ($P = .10$).

Conclusion: Deep learning automated phase error correction reduced inflow-outflow bias and variance of volumetric flow measurements in four-dimensional flow MRI, achieving results comparable with manual image-based phase error correction.

The visual and quantitative assessment of abdominopelvic hemodynamics is essential in the evaluation of many clinical entities. In abdominal imaging, this is primarily undertaken with Doppler US and time-resolved two-dimensional phase-contrast MRI (1). Abdominal US is limited by sonographic windows, but targeted windows can be applied to interrogate postoperative vascular complications of transplantation, renal artery stenosis, and other indications (2–4). Because of the need to place precise imaging planes at the time of the scan, planar phase-contrast MRI is challenging to implement in the clinical environment but can be used to evaluate mesenteric ischemia, aortic dissections, and other vascular conditions (5,6). Time-resolved three-dimensional (3D) phase-contrast MRI with three-directional velocity encoding (four-dimensional [4D] flow MRI) addresses these limitations by providing comprehensive imaging of the entire abdomen, allowing blood flow in any vessel to be retrospectively assessed in any direction (1,7,8).

While applications of 4D flow MRI have grown rapidly (9,10), the correction of magnetic eddy current–related background phase error remains a challenge (11–14). Partial phase error correction can be achieved using pre-emphasis techniques (15), incorporation of gradient nonlinearity in the image reconstruction process (16), and field derivation and correction via Maxwell equations (17); however, residual phase error may compromise the accuracy of 4D flow measurements (13,18). Further phase error correction is therefore required (Fig 1). Current methods primarily address residual phase error through one of two approaches: stationary phantom imaging and polynomial regression of phase error in static soft tissues (18). Phantom-based correction methods (19) require a second phantom scan after the patient scan with identical imaging parameters and are therefore impractical in a routine clinical setting (20). Image-based correction (14,21) can use pixel-based velocity thresholding throughout the cardiac cycle but often requires a human operator for reliable segmentation of static soft tissues.

Abbreviations

CNN = convolutional neural network, 4D = four-dimensional, LCIA = left common iliac artery, LCIV = left common iliac vein, RCIA = right common iliac artery, RCIV = right common iliac vein, 3D = three-dimensional

Summary

Deep learning-based background phase error correction improved the consistency of flow measurements in abdominopelvic four-dimensional flow MRI and simplified hemodynamic analysis for clinical use.

Key Results

- A deep learning algorithm trained with 99 abdominopelvic four-dimensional (4D) flow MRI examinations successfully generated phase error fields for automated correction.
- In an independent sample of 40 patients, flow measurements after deep learning correction had very strong correlation with manually corrected measurements ($\rho = 0.98$, $P < .001$).
- Automated correction reduced inflow-outflow bias and variance ($P < .001$), improving mean difference from −0.14 L/min uncorrected to 0.05 L/min deep learning corrected.

Convolutional neural networks (CNNs) are an emerging class of deep learning techniques that have been used for classification, localization, and segmentation and have broad potential to further benefit medical image analysis (22). Our objective was to develop a deep learning algorithm to generate phase error corrections without human intervention, simplifying the analysis and interpretation of abdominopelvic 4D flow acquisitions. We evaluated the feasibility of using a fully automated deep learning algorithm to perform image-based background phase error correction in 4D flow MRI and compared its effectiveness relative to manual image-based correction, applying inflow-outflow consistency as a principal benchmark of algorithm performance.

Materials and Methods

Patients

This study was compliant with the Health Insurance Portability and Accountability Act, and we obtained institutional review board approval, with waiver of informed consent. We retrospec-

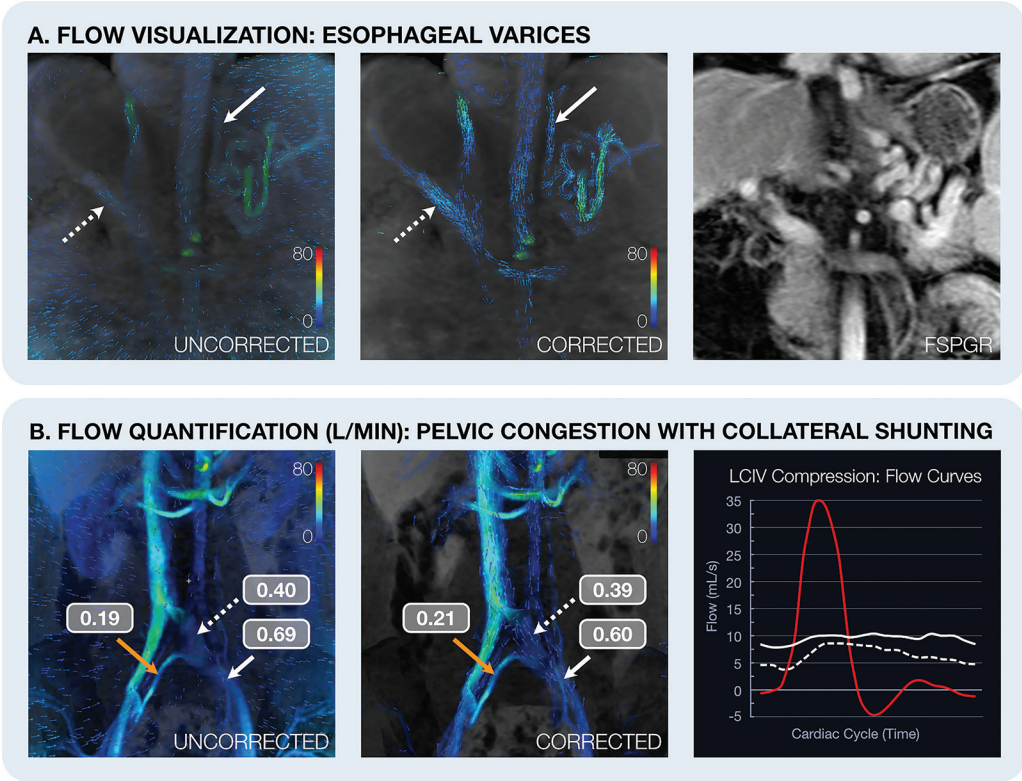

Figure 1: Effect of background phase error correction on flow visualization and quantification. **(A)** Coronal images in a 53-year-old man with cirrhosis and severe portal hypertension. Postcontrast four-dimensional (4D) flow MRI scans of the abdomen show portosystemic shunting through variceal vessels (solid arrows) that are difficult to discern prior to correction but are clearly seen after correction. The main portal vein (dashed arrows) is also better depicted. Adjacent anatomy is shown in the fast spoiled gradient echo (FSPGR) image. **(B)** Postcontrast 4D flow MRI scans in a 29-year-old woman with pelvic venous congestion, marked compression of the left common iliac vein (LCIV) under the right common iliac artery, and compensatory collateral flow connecting the LCIV to the right common iliac vein (RCIV). A large discrepancy in the amount of collateral flow (orange arrow) that passes to the RCIV is seen prior to correction. After correction, LCIV flow (0.60 L/min) is equal to the sum of flow within the compressed LCIV and the collateral vein (0.39 + 0.21 L/min). Line graph shows flow curves throughout one cardiac cycle for two locations in the LCIV, where right common iliac arterial flow (red line) suppresses venous return in the LCIV (dashed line and arrows). Venous flow in the LCIV before the collateral (solid line and arrows) remains unaffected.

Table 1: Imaging Parameters for Time-resolved 3D Phase-Contrast MRI with 3D Velocity Encoding

Parameter	Training Data Set (n = 85)	Validation Data Set (n = 14)	Testing Data Set (n = 40)
Temporal resolution (msec)	56 (38–175)	57 (45, 87)	56 (43, 74)
Spatial resolution (mm)			
Frequency	1.7 (1.3–2.5)	1.7 (1.6–2.0)	1.7 (1.6–1.9)
Phase	2.1 (1.7–3.0)	2.0 (1.9–2.4)	2.0 (1.9–2.3)
Section	3.0 (2.8–7.5)	2.8 (2.8–3.0)	2.8 (2.8–3.0)
Encoding velocity (cm/sec)	148 (80–200)	141 (80–250)	150 (80–250)
Acceleration factor			
Phase	3.0 (1.2–3.2)	3.0 (2.6–3.2)	3.0 (2.6–3.2)
Section	1.8 (1.2–2.0)	1.8 (1.8–2.0)	1.8 (1.8–2.0)
Scanning time (sec)	674 (409–810)	707 (630–808)	674 (357–840)
Contrast agent (%)			
Gadobutrol	78 (66/85)	86 (12/14)	90 (36/40)
Gadobenate dimeglumine	15 (13/85)	7 (1/14)	10 (4/40)
Gadoxetate disodium	7 (6/85)	0 (0/14)	0 (0/40)
Gadofosveset trisodium	0 (0/85)	7 (1/14)	0 (0/40)

Note.—Data for imaging parameters are presented as means, with ranges in parentheses. Data for contrast agents are presented as percentages, with raw data in parentheses. 3D – three-dimensional.

tively collected a convenience sample of 139 abdominopelvic 4D flow MRI acquisitions performed at our institution between January 2016 and July 2020 as part of routine clinical MRI examinations, which also included contrast-enhanced MR angiography and postcontrast fast spoiled gradient-echo imaging.

Data Acquisition

MRI examinations were performed on a 3-T MRI scanner (Discovery MR 750; GE Healthcare) using a 32-channel phased-array coil. Postcontrast 4D flow MRI was performed with a 3D cartesian strategy in which Ky-Kz samples were grouped in spiral-like sets and were acquired with golden angle ordering (23,24), evenly spaced over time (25) with dense central k-space sampling for respiratory soft gating (26). Imaging parameters are summarized in Table 1. The 4D flow MRI scans were acquired as a coronal slab through the abdomen and pelvis, with the patient's arms raised above his or her head to prevent soft-tissue wrapping in the right-left phase direction.

Manual Background Phase Error Correction

Manual phase error correction was performed with dedicated imaging software (Arterys, version 26.7.6; Arterys) by two individuals (S.Y., a 4th-year medical student; A.H., a board-certified radiologist with more than 10 years of experience working with 4D flow MRI). Manual correction was performed via segmentation of static tissue followed by patchwise linear regression of static tissue velocities. Raw uncorrected and corrected velocity data were exported from the imaging software.

Data Preprocessing

After 40 examinations were reserved for testing, the remaining 1980 temporal volumes from 99 examinations were randomly divided by examination into two cohorts, with 86% (85 of 99) for training and 14% (14 of 99) for validation. Maxwell terms and gradient field nonlinearity were corrected in-line during the image reconstruction process (16,17). After performing semiautomatic thresholding of magnitude images for exclusion of air pixels, velocity values corresponding to unexcluded pixels were used to generate a third-order polynomial regression of the manual correction. Velocities were scaled by the encoding velocity for each examination, and all data were downsampled to $64 \times 64 \times 64$ cubes due to anticipated GPU memory limitations.

Neural Network Training

Our 3D multichannel U-Net (27), a type of CNN whose architecture is illustrated in Figure 2, was trained for 300 epochs using mean squared error loss, hyperbolic tangent activation, and Adam optimization with a learning rate of 1×10^{-4}. Network training used TensorFlow-GPU 2.1 (Google) on a workstation running Ubuntu 18.04 (Canonical) equipped with four Nvidia Quadro GV100 GPUs (Nvidia). CNN design and training were performed by two authors (S.Y.; E.M.M., a doctoral student in his 6th year of training). The code for the model architecture and training routine is available on request (release version 1.0; *https://github.com/AiDALabUCSD/Abdominal-Phase-Error-Correction*; GitHub login required).

Polynomial Regression and Application

Pixelwise velocity corrections generated by the CNN were supplied as input to third-order polynomial least-squares regression after intensity thresholding for exclusion of air pixels. A single-phase error correction was generated for each examination, computed as the average of corrections generated for each of the 20 time points in the 4D flow time series. The fully automated postprocessing pipeline is shown in Figure 2.

Volumetric Flow Measurements

Segmentation of vessels for flow quantification was performed by two observers (S.Y., A.H.) for the infrarenal aorta in tripli-

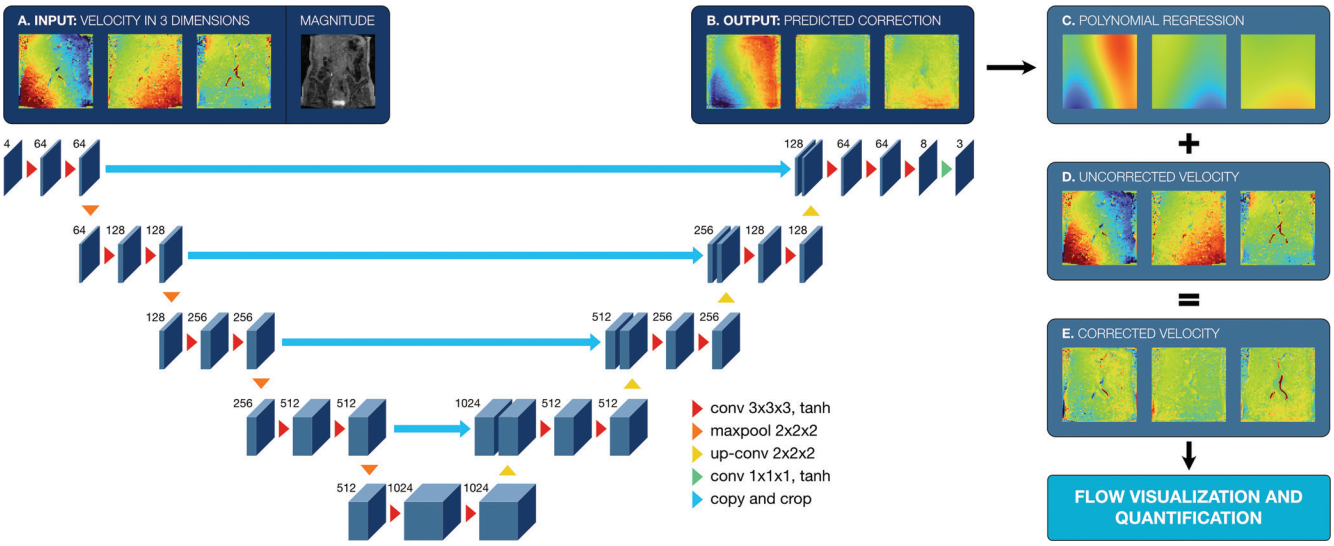

Figure 2: Pipeline for automated phase error correction. A three-dimensional (3D) multichannel U-Net (a type of convolutional neural network) designed with **(A)** four input channels, including flow velocities encoded in three cardinal directions and corresponding magnitude volumes, and **(B)** three output channels to infer corrections for the same three velocity components. Architecture of the 3D multichannel U-Net is shown, with numbers indicating the total number of channels, operations (arrowheads), and kernel sizes and activation functions indicated in the legend. As a postprocessing step, pixelwise inferred corrections are smoothed with least squares regression to a third-order polynomial in **(C)**. This correction is then added to the **(D)** original uncorrected data to generate **(E)** corrected flow data.

cate and individually for the left common iliac artery (LCIA) and right common iliac artery (RCIA), inferior vena cava, left common iliac vein (LCIV), and right common iliac vein (RCIV). The same manual segmentations were used for uncorrected, manually corrected, and automatically corrected data, such that measurements between the three data sets were spatially consistent.

Performance Evaluation

Internal consistency of flow measurements was established by assessing conservation of mass in the 40 test cases. The average of the three aortic measurements was compared with the sum of the LCIA and RCIA, while the inferior vena cava was compared with the sum of the LCIV and RCIV. Each arterial vessel was compared with its venous counterpart (aorta vs inferior vena cava, LCIA vs LCIV, and RCIA vs RCIV). A representative case from the test set is illustrated in Figure 3, showing the 24 total measurements per case.

Statistical Analysis

For the 40 test cases, *t* tests were performed with a difference of zero as the null hypothesis for the five comparisons assessing conservation of mass and a type I error threshold of $P < .01$ ($\alpha = .05$ with Bonferroni correction for multiple comparisons). Additional statistical comparisons were performed using the Bartlett test of homoscedasticity (28) followed by pairwise *F* tests with Bonferroni correction. These analyses were performed in RStudio 1.3.959 (R Foundation for Statistical Computing).

Inflow-outflow consistency in the test set was further assessed using Pearson correlation and Bland-Altman analysis. The time required for manual versus automated correction was assessed using a *t* test. We fitted a single-rater two-way random effects intraclass correlation model (29) to assess absolute agreement between flow measurements made by two observers (S.Y., A.H.). These statistical analyses were performed using the Scipy 1.4.1 and Pingouin 0.3.12 libraries in Python (version 3.7.7; *https://www.python.org/*).

Results

Patient Characteristics

We retrospectively collected abdominopelvic 4D flow MRI examinations from 140 patients (mean age, 47 years ± 14 [standard deviation]; 108 women). Patient characteristics grouped by clinical indication are summarized in Table 2.

Performance of Manual Phase Error Correction

Prior to background phase error correction, there was poor inflow-outflow consistency for comparison of arterial flow with venous flow and for comparison of blood flow before bifurcation with blood flow after bifurcation (Fig 3A, 3D). The mean absolute difference between flow measurements was 0.52 L/min ± 0.55 (standard deviation), while the mean percentage difference was 37% ± 26. Correlation between flow measurements was moderate ($\rho = 0.50$, $P < .001$).

After manual correction (Fig 3B, 3E), the mean absolute difference improved to 0.15 L/min ± 0.12, with a corresponding mean percentage difference of 14% ± 10. Corrected flow measurements also demonstrated very strong correlation between inflow and outflow measurements ($\rho = 0.94$, $P < .001$).

Clinical Application of 4D Flow

In Figure 4, we highlight two example cases in which manually corrected 4D flow MRI was helpful for diagnosis.

In the first example case (Fig 4A–4C), a 24-year-old woman with postural orthostatic tachycardia syndrome presented with orthostatic lightheadedness, left leg discomfort, and

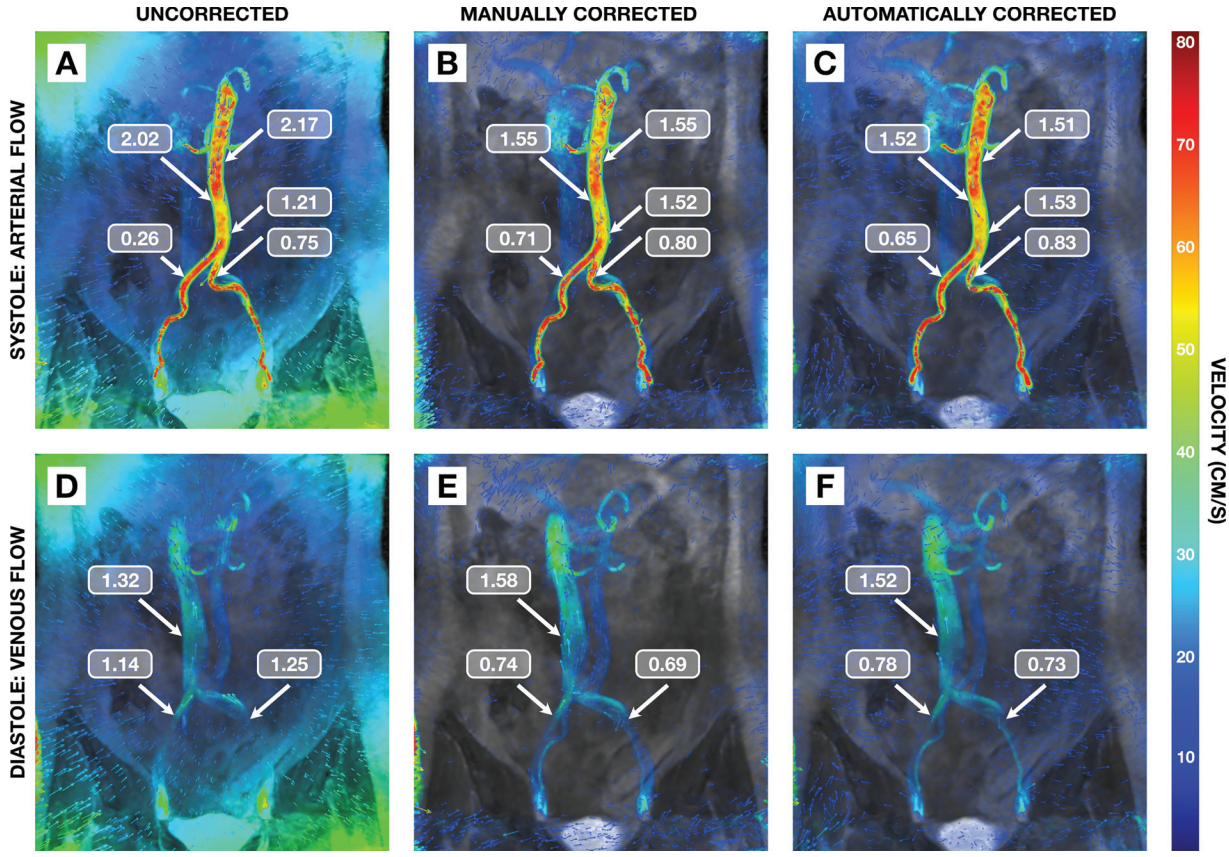

Figure 3: Visual example of background phase error correction for four-dimensional flow MRI. Images show visual and quantitative reduction of background phase error after manual or convolutional neural network (CNN)-based correction. **(A–C)** Coronal MRI scans of the aorta and common iliac arteries during peak systole. **(D–F)** Coronal MRI scans show the inferior vena cava and common iliac veins during mid-diastole. Flow velocity is represented by a color map ranging from blue (0 cm/sec) to red (80 cm/sec). For assessment of flow continuity, measurements (in liters per minute) were taken at multiple locations (arrows). Corrected velocity measurements showed improved consistency along the length of the infrarenal aorta and conservation of mass across bifurcations in the arterial and venous systems.

Table 2: Patient Characteristics

Parameter	Training Data Set (n = 85)	Validation Data Set (n = 14)	Testing Data Set (n = 40)	Total (n = 139)
Sex				
Female	63	10	35	108
Male	22	4	5	31
Age (y)*	48 ± 15	52 ± 15	43 ± 13	47 ± 14
Clinical indication				
Liver disease	25	4	6	35
Uterine bleeding and masses, including fibroids	30	3	21	54
Venous congestion	15	5	9	29
Mesenteric ischemia	6	0	0	6
Renal artery stenosis	9	2	4	15

Note.—Unless otherwise indicated, data are numbers of patients.
* Data are mean ± standard deviation.

abdominopelvic pressure that worsened throughout the day. She underwent multisequence MRI, including differential subsampling with cartesian ordering (30), which demonstrated dilated ovarian veins bilaterally and filling of pelvic venous collaterals. Further evaluation with 4D flow MRI enabled us to confirm retrograde flow in the left ovarian vein (280 mL/min) and anterograde flow in the right ovarian vein (230 mL/min). There was absent flow in the left renal vein as it passed under the superior mesenteric artery, indicating nutcracker physiology. There was limited flow (270 mL/min) in the LCIV as it passed under the RCIA, which was inadequate to accommodate the retrograde ovarian venous flow, indicating May-Thurner venous insufficiency.

The patient subsequently underwent catheter venography, which enabled us to confirm left ovarian vein reflux and left iliac venous insufficiency. This was followed by LCIV stenting, resolution of May-Thurner venous insufficiency and left leg discomfort, and, later, left gonadal vein embolization with resolution of her abdominal bloating, urinary discomfort, and pelvic pain.

In a second example case (Fig 4D–4F), an 89-year-old woman with a history of ischemic colitis underwent abdominal MRI for evaluation of persistent abdominal pain and diarrhea. Quantitative flow measurements using two-dimensional phase-contrast

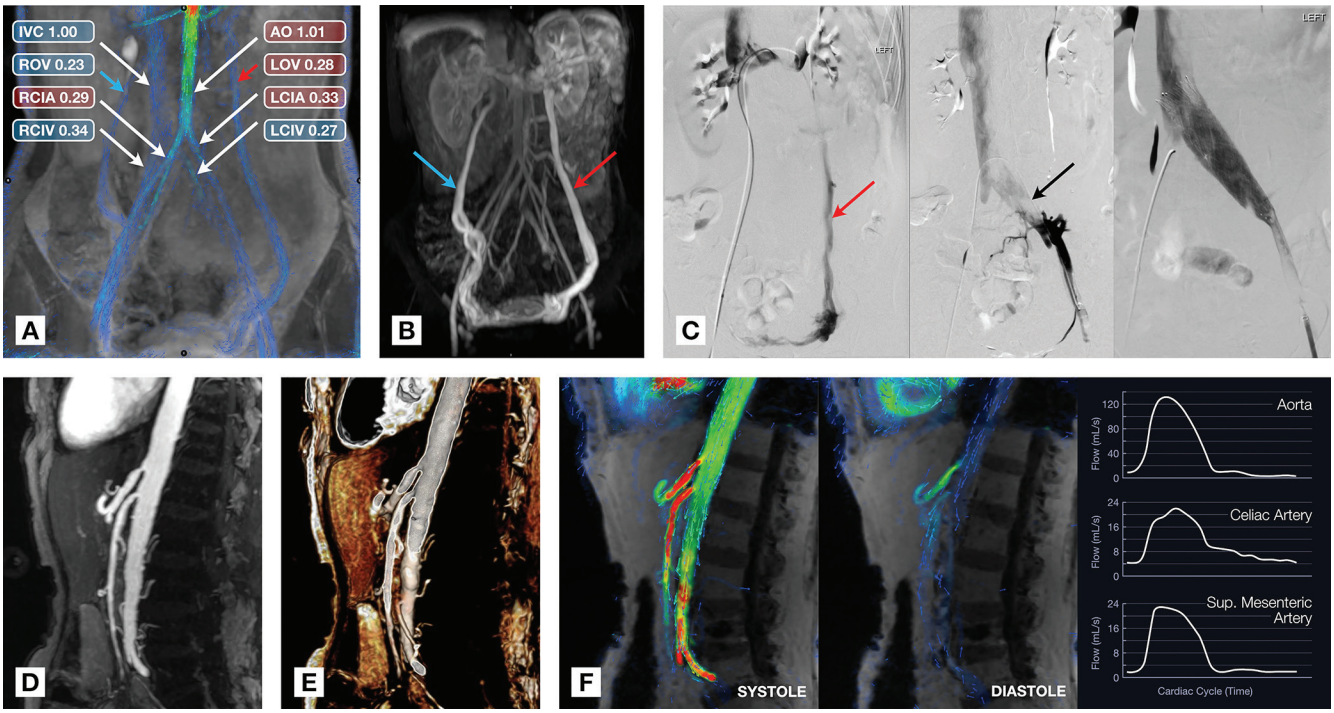

Figure 4: Clinical applications of abdominopelvic four-dimensional (4D) flow MRI. **(A–C)** Coronal oblique MRI scans obtained with postcontrast 4D flow MRI (**A**) and MR angiography (**B**) in a 24-year-old woman with Nutcracker syndrome and May-Thurner syndrome who had retrograde flow in an asymmetrically enlarged left ovarian vein (LOV) (red arrow) and antegrade flow in the enlarged contralateral ovarian vein (blue arrow). AO = aorta, IVC = inferior vena cava, LCIA = left common iliac artery, RCIA = right common iliac artery, RCIV = right common iliac vein, ROV = right ovarian vein. In **C,** both retrograde ovarian flow and left common iliac vein (LCIV) stenosis were confirmed during catheter angiography, with flow through the compressed LCIV (black arrow) being restored after stent placement. **(D–F)** Sagittal oblique images in an 89-year-old woman with a history of ischemic colitis and severe stenosis of the celiac artery and superior mesenteric artery at their origins, seen as focal vessel narrowing in the two-dimensional MR angiography image (**D**) and three-dimensional (3D) reconstruction (**E**). Postcontrast 4D flow MRI scan (**F**) shows similar narrowing and provides additional hemodynamic information: high flow velocity is shown in red, and persistent high-velocity flow in the celiac artery during diastole is reflected in the corresponding flow curves.

MRI demonstrated limited augmentation of mesenteric blood flow after a prandial challenge (5), with flow through the superior mesenteric vein increasing from 299 to 330 mL/min and flow through the superior mesenteric artery increasing from 386 to 414 mL/min. Postprandial 4D flow MRI measurements were obtained to assess the feasibility of using 4D flow in place of two-dimensional phase-contrast planes, and the 4D flow measurements were found to be similar to the two-dimensional phase-contrast flow measurements. We observed several additional findings on 4D flow MRI scans, including high-velocity systolic blood flow through the celiac (159.41 cm/sec) and superior mesenteric (136.33 cm/sec) arteries and prolonged diastolic forward flow through the stenotic celiac artery (Fig 4F). Taken together, these findings are consistent with hemodynamically significant celiac and superior mesenteric artery stenosis and chronic mesenteric ischemia.

Performance of Automated Phase Error Correction

Neural network inference required a mean of 0.54 second ± 0.01 per case, while postprocessing required a mean of 11.75 seconds ± 0.61 per case. The mean total time for automated phase error correction was 12.29 seconds ± 0.61 compared with manual phase error correction performed by the most experienced observer (A.H.), which required 152.3 seconds ± 52.58 per case ($P < .001$).

The multichannel 3D U-Net led to an improvement in inflow-outflow consistency comparable to that of manual correction, with strong correlation between flow measurements ($\rho = 0.91$, $P < .001$). The average standard deviation for the three aortic measurements performed for each case was 0.07 L/min, compared with 0.07 L/min after manual correction and 0.23 L/min for uncorrected cases. The CNN algorithm was successfully executed in all 40 test cases, resolving phase error in all three principal directions (Fig 5). There were no technical failures.

A direct comparison of flow measurements obtained using manual and automated correction demonstrated very strong correlation ($\rho = 0.98$, $P < .001$) (Fig 6A).

The multichannel 3D U-Net achieved an average difference between vessel measurements of 0.05 L/min overall ($P < .001$), an improvement over uncorrected measurements, which had an average difference of −0.14 L/min overall ($P = .01$). In comparison, manual correction had an average difference of 0.05 L/min ($P < .001$). When considering only comparisons of arterial flow versus venous flow, both correction methods showed marked improvement over uncorrected data, with mean differences of −0.005 L/min ($P = .79$) after manual correction and −0.003 L/min ($P = .89$) after automated correction compared with −0.35 L/min for uncorrected data ($P < .001$). Comparisons between pre- and postbifurcation flow also showed an improvement in mean difference from 0.17 L/min

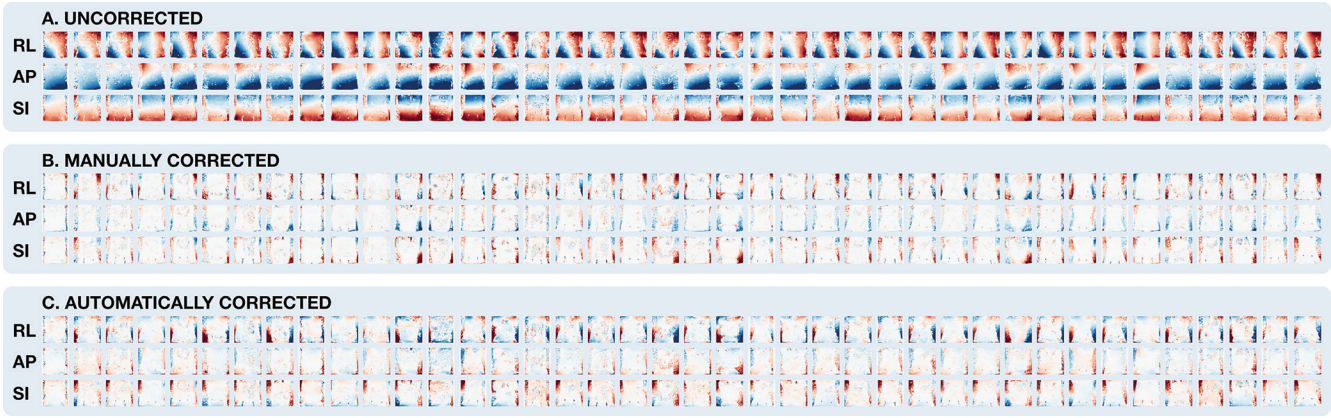

Figure 5: Representative coronal sections of MRI scans from all 40 test cases. With velocity shown on a red-white-blue color scale, manual and automated correction methods show a similar reduction of soft-tissue phase error, seen as primarily white coloring (zero flow). Phase errors for each cardinal direction appear to follow fairly consistent patterns but with slight differences from case to case. AP = anterior to posterior, RL = right to left, SI = superior to inferior.

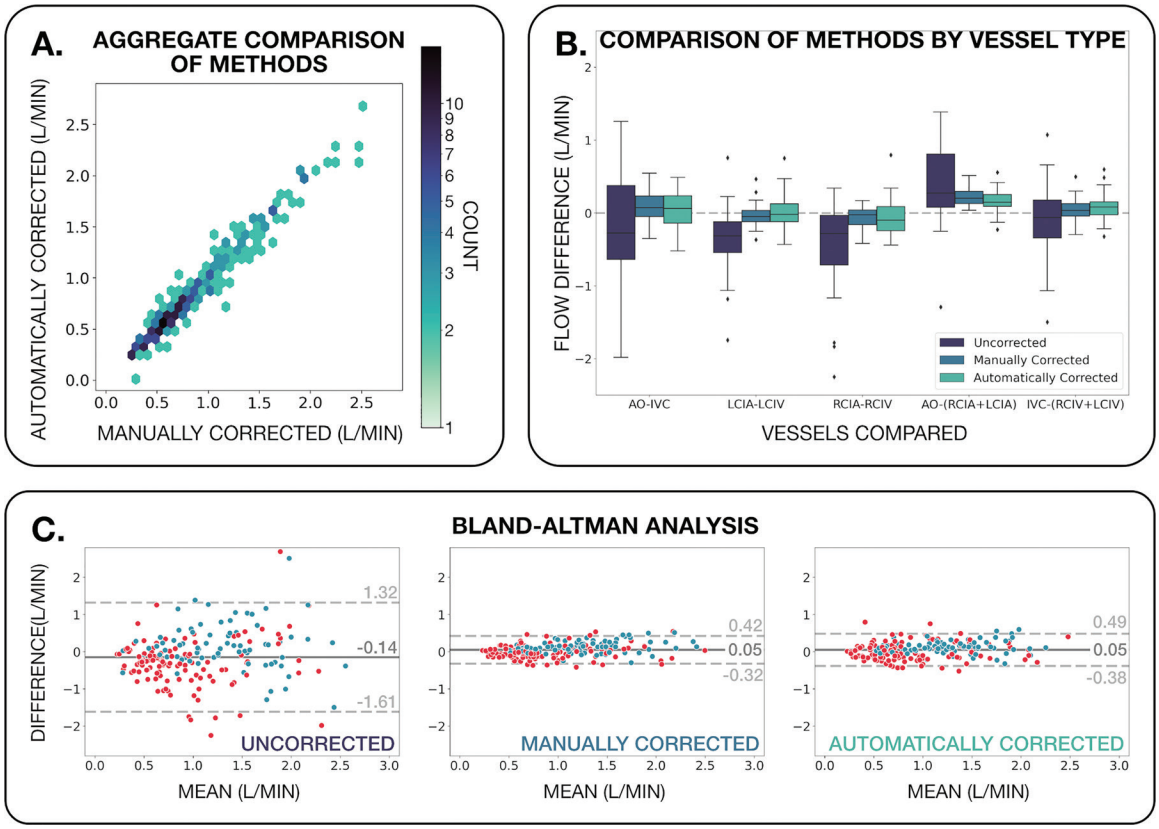

Figure 6: Analysis of volumetric flow continuity in the testing data set (40 examinations). **(A)** Panel shows a comparison of all manually and automatically corrected flow measurements. The slope of the regression is 1.01, and the correlation coefficient is 0.98. **(B)** Box-and-whisker plot grouped by vessel type compares uncorrected, manually corrected, and automatically corrected flow differences among the five vessel comparisons. Compared with uncorrected measurements, manually and automatically corrected measurements show an overall reduction in range, with mean values closer to zero. AO = aorta, IVC = inferior vena cava, LCIA = left common iliac artery, LCIV = left common iliac vein, RCIA = right common iliac artery, RCIV = right common iliac vein. **(C)** Bland-Altman plots with comparisons of arterial and venous flow (red) and comparisons of flow before and after bifurcation (blue) show greater flow consistency with narrower limits of agreement after both manual and automated correction.

uncorrected to 0.14 L/min manually corrected and 0.13 automatically corrected, though the mean difference remained greater than zero for both correction methods (P = .02 for uncorrected, $P < .001$ for manually corrected, $P < .001$ for automatically corrected). Uncorrected data demonstrated a mean difference significantly different from zero for three of the five vessel comparisons ($P < .001$ for the difference between the LCIA and LCIV, the difference between the RCIA and RCIV, and the difference between the aorta and the sum of the RCIA and LCIA, while manually and automatically corrected vessel comparisons were significantly different from zero ($P < .001$ and $P < .001$, respectively)

Table 3: Effect of Manual and Deep Learning–based Automated Phase Error Correction on Inflow-Outflow Consistency for Five Vessel Comparisons

	Uncorrected		Manually Corrected		Automatically Corrected	
Vessel Comparison	Mean	*P* Value	Mean	*P* Value	Mean	*P* Value
AO to IVC	–0.27 (–0.62, 0.08)	.13	0.08 (0.01, 0.15)	.03	0.05 (0.03, 0.12)	.21
LCIA to LCIV	–0.38 (–0.52,–0.24)	<.001	–0.03 (–0.07, 0.02)	.23	0.03 (–0.04, 0.10)	.41
RCIA to RCIV	–0.42 (–0.60,–0.24)	<.001	–0.07 (–0.12,–0.02)	.01	–0.07 (–0.15, 0.01)	.09
AO to sum of RCIA and LCIA	0.44 (0.24, 0.64)	<.001	0.22 (0.19, 0.26)	<.001	0.17 (0.12, 0.22)	<.001
IVC to sum of RCIV and LCIV	–0.10 (–0.25, 0.06)	.22	0.05 (0.002, 0.10)	.04	0.08 (0.03, 0.14)	.005

Note.—Data in parentheses are 95% CIs. Listed *P* values correspond to *t* tests. AO = aorta, IVC = inferior vena cava, LCIA = left common iliac artery, LCIV = left common iliac vein, RCIA = right common iliac artery, RCIV = right common iliac vein.

for only the difference between the aorta and the sum of the RCIA and LCIA (Table 3, Fig 6B).

Manual and automated correction methods also demonstrated a reduction in variance of volumetric flow differences, with overall mean difference as follows: −0.14 L/min (95% limits of agreement: −1.61, 1.32) for uncorrected data, 0.05 L/min (95% limits of agreement: −0.32, 0.42) for manually corrected data, and 0.05 L/min (95% limits of agreement: −0.38, 0.49) for automatically corrected data (Fig 6C). The Bartlett test of homogeneity of variances yielded an overall $P < .001$, and pairwise *F* tests with Bonferroni correction demonstrated no significant difference between manual and automated correction ($P < .001$ for manually corrected vs uncorrected data, $P < .001$ for automatically corrected vs uncorrected data, $P = .10$ for manual vs automatically corrected data).

Analysis of interobserver variability demonstrated excellent reliability both before and after background phase error correction. The intraclass correlation coefficient prior to correction was 0.94 ($P < .001$). Manual and automated correction methods each improved the coefficient to 0.99 ($P < .001$ for both).

Discussion

Four-dimensional (4D) flow MRI has become increasingly valuable in the qualitative and quantitative assessment of blood flow. Since all measurements can be retrospectively obtained after image acquisition without the need for targeted US windows or placement of two-dimensional phase-contrast planes at the time of the examination, 4D flow MRI provides versatility that can be essential in the diagnostic process. However, the correction of magnetic eddy current–related background phase error remains a challenge in abdominal applications.

In this study, we demonstrated the feasibility of automating background phase error correction using a multichannel 3D U-Net, with improved consistency in comparisons of arterial and venous flow as well as in comparisons of blood flow before and after bifurcations. In a test set of 40 patients, automated phase error correction demonstrated very strong correlation with manually corrected measurements ($\rho = 0.98$, $P < .001$). Inflow-outflow bias and variance were also reduced, with mean difference and limits of agreement improving from −0.14 L/min (95% limits of agreement: −1.61, 1.32) (uncorrected) to 0.05 L/min (95% limits of agreement: −0.38, 0.49) (automatically corrected) and no significant difference in variance between manual and automated correction methods ($P = .10$, *F* test with Bonferroni correction).

Performance of manual correction requires substantial time and expertise due to the need for manual vessel segmentation. Previous studies (18,31) have explored the effect of various parameters on the accuracy of image-based phase error correction, including the signal-to-noise ratio of the data itself, the percentage of stationary tissue used in the regression, and the spatial order of the regressed correction. In general, the quality of the correction decreases with decreasing percentage of static tissue, which means that manual tissue segmentation requires a delicate balance between excluding as many vessels as possible and maximizing inclusion of soft tissue. This deterioration is increasingly pronounced with regressions of higher spatial order; in fact, third- and sometimes second-order polynomial regressions are frequently rendered impossible due to insufficient soft-tissue selection. CNNs are able to overcome this limitation because they learn relevant features of input images on their own.

Our study had limitations. First, our training and testing data were sourced using one MRI scanner from one vendor at one institution. Second, because many of our patients underwent 4D flow MRI for clinical evaluation of venous abnormalities, low encoding velocity (usually 80 cm/sec) created velocity aliasing within some high-flow arteries, limiting our ability to accurately measure blood flow in some vessels. Although we did not evaluate the potential of CNNs to correct for velocity aliasing, it is plausible that they might be applied similarly for this purpose as well. Finally, performance evaluation of our neural network relied on inflow-outflow consistency in major abdominal vessels. We did not assess whether detection of intraabdominal shunts was impaired or improved with phase error correction, instead focusing primarily on the feasibility of using a CNN to perform this correction.

In conclusion, correction of background phase offset poses a challenge to the clinical application of four-dimensional (4D) flow MRI but can be accomplished using a single multichannel three-dimensional U-Net, a type of convolutional neural network (CNN). We expect that similar results may be possible for other body territories, scanners, vendors, and institutions, which might be the subject of future investigations. This could

be accomplished by retraining the CNN using new 4D flow data sets or by using transfer learning to expand the generalizability of this CNN. Our proof-of-concept study demonstrates the feasibility of automating phase error correction, bypassing the segmentation that is generally required for manual correction. In essence, we have trained a CNN to perform a complex task, simultaneously capturing the phase error in static soft tissue while ignoring flowing blood in the arterial and venous systems. The feasibility of this work highlights the untapped potential of CNNs to accomplish complex visual and computational tasks that may not be readily performed by humans and may help bring advanced imaging technologies, including 4D flow MRI, into routine clinical care.

Acknowledgments: We acknowledge Microsoft AI for Health for computational resources used for CNN training.

Author contributions: Guarantors of integrity of entire study, S.Y., A.C.R., A.H.; study concepts/study design or data acquisition or data analysis/interpretation, all authors; manuscript drafting or manuscript revision for important intellectual content, all authors; approval of final version of submitted manuscript, all authors; agrees to ensure any questions related to the work are appropriately resolved, all authors; literature research, S.Y., E.M.M., P.R.T., A.C.R., A.H.; experimental studies, S.Y., E.M.M., M.T.A., A.H.; statistical analysis, S.Y., E.M.M.; and manuscript editing, S.Y., E.M.M., S.S.V., P.R.T., J.L., A.C.R., A.H.

Disclosures of conflicts of interest: **S.Y.** disclosed no relevant relationships. **E.M.M.** disclosed no relevant relationships. **M.T.A.** stock options in Arterys. **S.S.V.** equity interest in Arterys, Inkspace, and Heartvista. **P.R.T.** consulting fees from Amgen, Novo-Nordisk, Medtronic, Boehringer-Ingelheim, Sanofi, and Esperion Therapeutics; shareholder in Epirium Bio. **J.L.** disclosed no relevant relationships. **A.C.R.** disclosed no relevant relationships. **A.H.** grants from GE Healthcare and Bayer unrelated to the present work; patent filed by Stanford University and licensed by multiple vendors related to phase-error correction and analysis of 4D flow MRI; cofounder of and shareholder in Arterys.

References

1. Dyverfeldt P, Bissell M, Barker AJ, et al. 4D flow cardiovascular magnetic resonance consensus statement. J Cardiovasc Magn Reson 2015;17(1):72.
2. Rafailidis V, Fang C, Yusuf GT, Huang DY, Sidhu PS. Contrast-enhanced ultrasound (CEUS) of the abdominal vasculature. Abdom Radiol (NY) 2018;43(4):934–947.
3. Nicolau C, Ripollés T. Contrast-enhanced ultrasound in abdominal imaging. Abdom Imaging 2012;37(1):1–19.
4. Brkic A, Terslev L, Møller Døhn U, Torp-Pedersen S, Schmidt WA, Diamantopoulos AP. Clinical Applicability of Ultrasound in Systemic Large Vessel Vasculitides. Arthritis Rheumatol 2019;71(11):1780–1787.
5. Li KC, Whitney WS, McDonnell CH, et al. Chronic mesenteric ischemia: evaluation with phase-contrast cine MR imaging. Radiology 1994;190(1): 175–179.
6. Pelc NJ, Herfkens RJ, Shimakawa A, Enzmann DR. Phase contrast cine magnetic resonance imaging. Magn Reson Q 1991;7(4):229–254.
7. Roldán-Alzate A, Francois CJ, Wieben O, Reeder SB. Emerging Applications of Abdominal 4D Flow MRI. AJR Am J Roentgenol 2016;207(1):58–66.
8. Markl M, Frydrychowicz A, Kozerke S, Hope M, Wieben O. 4D flow MRI. J Magn Reson Imaging 2012;36(5):1015–1036.
9. Hope MD, Sedlic T, Dyverfeldt P. Cardiothoracic magnetic resonance flow imaging. J Thorac Imaging 2013;28(4):217–230.
10. Pereira VM, Delattre B, Brina O, Bouillot P, Vargas MI. 4D Flow MRI in Neuroradiology: Techniques and Applications. Top Magn Reson Imaging 2016;25(2):81–87.
11. Callaghan FM, Burkhardt B, Geiger J, Valsangiacomo Buechel ER, Kellenberger CJ. Flow quantification dependency on background phase correction techniques in 4D-flow MRI. Magn Reson Med 2020;83(6):2264–2275.
12. Viola F, Dyverfeldt P, Carlhäll CJ, Ebbers T. Data Quality and Optimal Background Correction Order of Respiratory-Gated k-Space Segmented Spoiled Gradient Echo (SGRE) and Echo Planar Imaging (EPI)-Based 4D Flow MRI. J Magn Reson Imaging 2020;51(3):885–896.
13. Gatehouse PD, Rolf MP, Graves MJ, et al. Flow measurement by cardiovascular magnetic resonance: a multi-centre multi-vendor study of background phase offset errors that can compromise the accuracy of derived regurgitant or shunt flow measurements. J Cardiovasc Magn Reson 2010;12(1):5.
14. Hofman MBM, Rodenburg MJA, Markenroth Bloch K, et al. In-vivo validation of interpolation-based phase offset correction in cardiovascular magnetic resonance flow quantification: a multi-vendor, multi-center study. J Cardiovasc Magn Reson 2019;21(1):30.
15. Jehenson P, Westphal M, Schuff N. Analytical method for the compensation of eddy-current effects induced by pulsed magnetic field gradients in NMR systems. J Magn Reson (1969) 1990;90(2):264–278.
16. Markl M, Bammer R, Alley MT, et al. Generalized reconstruction of phase contrast MRI: analysis and correction of the effect of gradient field distortions. Magn Reson Med 2003;50(4):791–801.
17. Bernstein MA, Zhou XJ, Polzin JA, et al. Concomitant gradient terms in phase contrast MR: analysis and correction. Magn Reson Med 1998;39(2):300–308.
18. Busch J, Giese D, Kozerke S. Image-based background phase error correction in 4D flow MRI revisited. J Magn Reson Imaging 2017;46(5):1516–1525.
19. Chernobelsky A, Shubayev O, Comeau CR, Wolff SD. Baseline correction of phase contrast images improves quantification of blood flow in the great vessels. J Cardiovasc Magn Reson 2007;9(4):681–685.
20. Gatehouse PD, Rolf MP, Bloch KM, et al. A multi-center inter-manufacturer study of the temporal stability of phase-contrast velocity mapping background offset errors. J Cardiovasc Magn Reson 2012;14(1):72.
21. Walker PG, Cranney GB, Scheidegger MB, Waseleski G, Pohost GM, Yoganathan AP. Semiautomated method for noise reduction and background phase error correction in MR phase velocity data. J Magn Reson Imaging 1993;3(3):521–530.
22. Soffer S, Ben-Cohen A, Shimon O, Amitai MM, Greenspan H, Klang E. Convolutional neural networks for radiologic images: a radiologist's guide. Radiology 2019;290(3):590–606.
23. Cheng JY, Zhang T, Ruangwattanapaisarn N, et al. Free-breathing pediatric MRI with nonrigid motion correction and acceleration. J Magn Reson Imaging 2015;42(2):407–420.
24. Cheng JY, Hanneman K, Zhang T, et al. Comprehensive motion-compensated highly accelerated 4D flow MRI with ferumoxytol enhancement for pediatric congenital heart disease. J Magn Reson Imaging 2016;43(6):1355–1368.
25. Winkelmann S, Schaeffter T, Koehler T, Eggers H, Doessel O. An optimal radial profile order based on the Golden Ratio for time-resolved MRI. IEEE Trans Med Imaging 2007;26(1):68–76.
26. Cheng JY, Alley MT, Cunningham CH, Vasanawala SS, Pauly JM, Lustig M. Nonrigid motion correction in 3D using autofocusing with localized linear translations. Magn Reson Med 2012;68(6):1785–1797.
27. Ronneberger O, Fischer P, Brox T. U-Net: Convolutional Networks for Biomedical Image Segmentation. In: Navab N, Hornegger J, Wells W, Frangi A, eds. Medical Image Computing and Computer-Assisted Intervention – MICCAI 2015. MICCAI 2015. Lecture Notes in Computer Science, vol 9351. Cham, Switzerland: Springer, 2015; 234–241.
28. Lim TS, Loh WY. A comparison of tests of equality of variances. Comput Stat Data Anal 1996;22(3):287–301.
29. Shrout PE, Fleiss JL. Intraclass correlations: uses in assessing rater reliability. Psychol Bull 1979;86(2):420–428.
30. Saranathan M, Rettmann DW, Hargreaves BA, Clarke SE, Vasanawala SS. DIfferential Subsampling with Cartesian Ordering (DISCO): a high spatio-temporal resolution Dixon imaging sequence for multiphasic contrast enhanced abdominal imaging. J Magn Reson Imaging 2012;35(6):1484–1492.
31. Keller EJ, Collins JD, Rigsby C, Carr JC, Markl M, Schnell S. Superior Abdominal 4D Flow MRI Data Consistency with Adjusted Preprocessing Workflow and Noncontrast Acquisitions. Acad Radiol 2017;24(3):350–358.